Glypican-3–Targeting F(ab′)2 for ^{89}Zr PET of Hepatocellular Carcinoma

Jonathan G. Sham[1], Forrest M. Kievit[2], John R. Grierson[3], Peter A. Chiarelli[2], Robert S. Miyaoka[3], Miqin Zhang[4], Raymond S. Yeung[1], Satoshi Minoshima[3], and James O. Park[1]

[1]Department of Surgery, University of Washington, Seattle, Washington; [2]Department of Neurological Surgery, University of Washington, Seattle, Washington; [3]Department of Radiology, University of Washington, Seattle, Washington; and [4]Department of Materials Science & Engineering, University of Washington, Seattle, Washington

Hepatocellular carcinoma (HCC) is an increasingly lethal malignancy for which management is critically dependent on accurate imaging. Glypican-3 (GPC3) is a cell surface receptor overexpressed in most HCCs and provides a unique target for molecular diagnostics. The use of monoclonal antibodies (mAbs) that target GPC3 (αGPC3) in PET imaging has shown promise but comes with inherent limitations associated with mAbs such as long circulation times. This study used ^{89}Zr-conjugated F(ab′)2 fragments directed against GPC3 (^{89}Zr-αGPC3-F(ab′)2) to evaluate the feasibility of the fragments as a diagnostic immuno-PET imaging probe. **Methods:** Immobilized ficin was used to digest αGPC3, creating αGPC3-F(ab′)2 fragments subsequently conjugated to ^{89}Zr. In vivo biodistribution and PET studies were performed on GPC3-expressing HepG2 and GPC3-nonexpressing RH7777 orthotopic xenografts. **Results:** Reliable αGPC3-F(ab′)2 production via immobilized ficin digestion was verified by high-performance liquid chromatography and sodium dodecyl sulfate polyacrylamide gel electrophoresis. ^{89}Zr-αGPC3-F(ab′)2 demonstrated F(ab′)2-dependent, antigen-specific cell binding. HepG2 tumor uptake was higher than any other tissue, peaking at 100 ± 21 percentage injected dose per gram (%ID/g) 24 h after injection, a value 33- to 38-fold higher than GPC3-nonexpressing RH7777 tumors. The blood half-life of the ^{89}Zr-αGPC3-F(ab′)2 conjugate was approximately 11 h, compared with approximately 115 h for historic mAb controls. This shorter half-life enabled clear tumor visualization on PET 4 h after administration, with a resultant peak tumor-to-liver contrast ratio of 23.3. Blocking antigen-expressing tumors with an excess of nonradiolabeled αGPC3 resulted in decreased tumor uptake similar to native liver. The kidneys exhibited high tissue uptake, peaking at 24 h with 83 ± 12 %ID/g. HepG2 tumors ranging from 1.5 to 7 mm were clearly visible on PET, whereas larger RH7777 tumors displayed signal lower than background liver tissue. **Conclusion:** This study demonstrates the feasibility of using ^{89}Zr-αGPC3-F(ab′)2 for intrahepatic tumor localization with small-animal PET. Faster blood clearance and lower background liver uptake enable excellent signal-to-noise ratios at early time points. Increased renal uptake is similar to that as has been seen with clinical radioactive peptide imaging. ^{89}Zr-αGPC3-F(ab′)2 addresses some of the shortcomings of whole-antibody immuno-PET probes. Further optimization is warranted to maximize probe sensitivity and specificity in the process of clinical translation.

Key Words: F(ab′)2; glypican-3; ^{89}Zr; positron emission tomography (PET); hepatocellular carcinoma (HCC)

J Nucl Med 2014; 55:2032–2037
DOI: 10.2967/jnumed.114.145102

Hepatocellular carcinoma (HCC) recently emerged as the second leading cause of cancer death globally (*1,2*). Radiographic imaging is essential in diagnosing HCC, often abrogating the need for biopsy and tissue diagnosis (*3,4*). However, standard multiphase CT and MR imaging have limited spatial resolution and lack tissue specificity (*5–8*). Our group recently reported the use of a ^{89}Zr-conjugated monoclonal antibody (mAb) targeting the HCC-specific marker glypican-3 (GPC3) to address these limitations of conventional imaging approaches (*9*). Although demonstrating excellent sensitivity and specificity, the use of intact mAbs for targeted molecular imaging presents its own shortcomings. Because of their relatively large size and intact Fc region, mAbs have long blood half-lives leading to suboptimal imaging pharmacokinetics, poorer tumor penetration, and increased immunogenicity (*10–14*).

Smaller targeting moieties such as F(ab′)2 fragments have emerged as an alternative to mAbs in an attempt to overcome the aforementioned limitations (*15–20*). Removal of the Fc region either through enzymatic digestion of the parent mAb or through protein engineering significantly reduces interactions with native Fc receptors and resultant nonspecific binding (*21*), potentially improving image quality. Compared with mAbs, the smaller size of F(ab′)2 (~110 vs. ~150 kD) dramatically impacts its in vivo pharmacokinetics. The blood clearance of F(ab′)2 is significantly faster than whole-mAb conjugates, leading to blood half-lives measured in hours rather than days (*22–25*). This rapid clearance leads to higher tumor-to-background ratios at earlier time points, allowing for a more clinically practical PET contrast agent. Although most whole-mAb immuno-PET conjugates require 3–5 d to achieve acceptable signal-to-noise ratios (*9,26–28*), F(ab′)2 conjugates can demonstrate similar imaging performance just hours after administration, theoretically allowing for same-day administration and imaging (*17,19*).

The immune system's interaction with mAb-based theranostics has been a long-standing hurdle for clinical oncology applications (*29*). The patient-mounted humoral response against the Fc domain of mAb targeting moieties can severely limit repeated imaging or treatment directed against the same antigen (*30*). Their smaller

Received Jul. 1, 2014; revision accepted Sep. 8, 2014.
For correspondence or reprints contact: James O. Park, 1959 NE Pacific St., P.O. Box 356410, Seattle, WA 98195-6410.
E-mail: jopark@uw.edu
Published online Oct. 30, 2014.

size, rapid blood clearance, and lack of Fc domain decrease the immunogenic potential of F(ab′)2-based radioconjugates, providing an instrument to enhance the safety and efficacy of repeated administrations. Additionally, F(ab′)2 fragments enable deeper penetration of the conjugated radioisotope into the tumor microenvironment, facilitating more accurate imaging and enhanced therapeutic efficacy (*22,24*).

Our recent work with ^{89}Zr PET imaging of HCC using an anti-GPC3 mAb (αGPC3) has shown promise (*9*), although ^{89}Zr-αGPC3 suffers from the same shortcomings as other mAb-based imaging probes. Its long blood half-life and relatively high background liver uptake hinders tumor-to-background ratios at early time points, necessitating an imaging delay of approximately 72 h to act as an effective contrast agent. As continuation and advancement of this work, we herein report the development of a ^{89}Zr PET imaging probe that uses the F(ab′)2 region of αGPC3 to address several limitations imposed by the whole-αGPC3 targeting moiety. This serves as a proof-of-concept study for the use of ^{89}Zr-αGPC3-F(ab′)2 fragments to image HCC in an attempt to explore the potential for a more clinically suitable contrast agent.

MATERIALS AND METHODS

Cell Lines and Tissue Culture

Luciferase-expressing GPC3-positive HepG2 HCC cells were purchased from PerkinElmer (Bioware HT1080-luc2), and GPC3-negative RH7777 HCC cells were purchased from American Type Culture Collection (no. CRL-1601).

Generation of αGPC3 F(ab′)2 Fragments and ^{89}Zr Labeling

αGPC3 IgG_1-producing hybridomas were generated using previously described methods through the Fred Hutchison Cancer Research Center antibody core (*31*). To generate F(ab′)2 fragments, whole antibody was incubated with immobilized ficin (Pierce Biotechnology) and 4 mM cysteine in 0.1 M citrate buffer for 35 h at 37°C. F(ab′)2 product was purified using high-performance liquid chromatography (HPLC) (phosphate-buffered saline, pH 7.4; Superdex-200 10/300 GL [GE Healthcare]). Fragment size and composition were confirmed with analytic HPLC and sodium dodecyl sulfate polyacrylamide gel electrophoresis (SDS-PAGE) gels. ^{89}Zr-αGPC3-F(ab′)2 labeling was performed by an adaptation of the Vosjan protocol (*32*), not requiring extraordinary trace demetalation of materials. Details are found in the supplemental data (available at http://jnm.snmjournals.org).

Determination of αGPC3 Whole-Antibody and F(ab′)2 Affinity

Affinity measurements were performed using a ForteBio OctetRED96 (Pall Life Sciences) by the Vanderbilt Antibody and Protein Resource through the Vanderbilt Institute of Chemical Biology and the Vanderbilt Ingram Cancer Center (P30 CA68485). Purified human carrier-free glypican-3 protein (R&D Biosystems) was used as the antigen target.

Animal Models

All animal studies were performed in accordance with the University of Washington Office of Animal Welfare guidelines for the humane use of animals, and all procedures were reviewed and approved by the Institutional Animal Care and Use Committee. Orthotopic xenografts were created as previously described (*9*). Briefly, 8-wk-old female athymic Nu/J mice (Jackson Laboratories) were anesthetized using 1.5% inhaled isoflurane, and the left lobe of the liver was exposed through an upper midline laparotomy. HCC cells (2×10^6) in 50 μL of Dulbecco modified Eagle medium containing 50% Matrigel (BD Biosciences) were injected into the subcapsular space of the left lobe. Four weeks after HepG2 and 2 wk after RH7777 cell injection, Vivoglo luciferin (75 mg/kg) (Promega) was administered by intraperitoneal injection and imaged using an IVIS Lumina II imaging system (PerkinElmer) to monitor the growth of intrahepatic tumors.

Small-Animal PET

Imaging studies were performed using the Siemens Inveon PET scanner. Whole-body imaging was performed on mice on a temperature-controlled bed, anesthetized with 1.5%–2.5% isoflurane with real-time respiratory monitoring. Tumor-bearing mice selected by IVIS imaging were injected with approximately 7.4 MBq (200 μCi) of ^{89}Zr-αGPC3-F(ab′)2 (~50 ug antibody) via the tail vein. Control animals ($n = 3$) were coinjected with 1 mg of unlabeled αGPC3 as a competition assay. Imaging time points (duration) were as follows: 4 h (20 min), 24 h (30 min), and 72 h (60 min). Details are found in the supplemental data.

Biodistribution

All animals were injected with approximately 7.4 MBq of ^{89}Zr-αGPC3-F(ab′)2 (~50 μg antibody) via the tail vein. Tissue biodistribution was determined in HepG2 and RH7777 tumor–bearing animals 4, 24, and 72 h after injection ($n = 5$ each). Three additional HepG2-bearing mice were coinjected with 1 mg of unlabeled whole αGPC3 as blocked controls. At the designated times, animals were euthanized and the whole body perfused with 50 mL of lactated ringers as previously described (*33*). Tumor, blood, and selected organs were harvested and wet-weighed, and radioactivity was measured using a Cobra II auto γ counter (Packard) channeled for 0.908-MeV γ (100%) rays. PET biodistribution mean activity data were obtained using a 0.02 cm^2 circular region of interest with 596.3-μm slice thickness. Details are found in the supplemental data.

Statistical Analysis

All numeric data for animal groups are expressed as the average value ± the SD unless otherwise indicated. When expressing data for individual animals, the SD represents the distribution of the data within the measured region of interest. Excel (version 12.3.6; Microsoft) was used for statistical analysis. The blood half-life was calculated using a best-fit exponential decay function in Excel. An unpaired, 2-tailed, Student t test was used with a P value of less than 0.05 considered statistically significant.

RESULTS

F(ab′)2 Production

Twenty milligrams of αGPC3 IgG_1 were incubated for 35 h with immobilized ficin in 0.1 M citrate buffer containing 4 mM cysteine. HPLC fractionation and purification (phosphate-buffered saline, pH 7.4; Superdex-200 10/300 GL) of the digestion product was performed (Fig. 1A). The primary peak seen at 13.3 min composed of αGPC3-F(ab′)2 fragments was collected, whereas later small-molecular-weight peaks representing digested Fc fragments and other debris were discarded. F(ab′)2 (3.8 mg) was recovered, representing a 26% yield. HPLC performed after F(ab′)2 conjugation with isothiocyanotobenzyldesferrioxamine confirmed uniformity of the labeled substrate (Fig. 1B). Finally, γ-radioactivity-detection HPLC was performed after radiolabeling of F(ab′)2 with ^{89}Zr (Fig. 1C). A leading shoulder constituting a small proportion of the overall sample can be seen in the postlabeling tracing, most likely representing F(ab′)2 that dimerized during the radiolabeling process.

SDS-PAGE was performed using unconjugated αGPC3 and F(ab′)2 to further validate fragment size and composition (Fig. 1D). Nonreduced, denatured αGPC3 and F(ab′)2 appear as bands at the expected sizes of approximately 155 and approximately 110 kDa, respectively. Once reduced, αGPC3 reveals bands at approximately 50 and

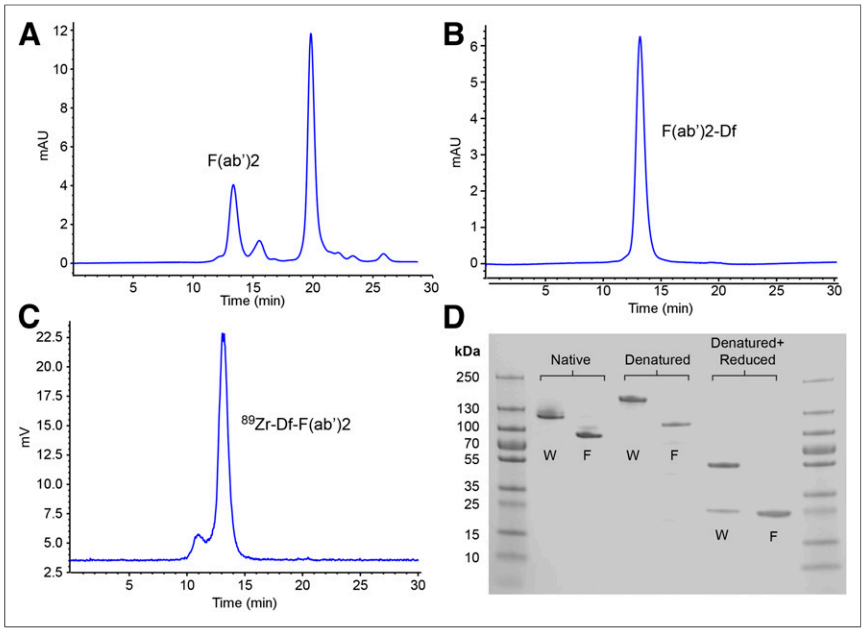

FIGURE 1. HPLC tracings performed on αGPC3 and immobilized ficin digestion product (A), F(ab')2 conjugate (B), and radiolabeled ^{89}Zr-F(ab')2 (C). (D) SDS-PAGE of undigested αGPC3 (W) and F(ab')2 (F) under native, denatured, and denatured + reduced conditions. Df = isothiocyanotobenzyldesferrioxamine.

approximately 25 kDa, representing the heavy and light chains constituting typical IgG_1. Reduced F(ab′)2 demonstrates a single large band at approximately 25 kDa consistent with a true F(ab′)2 fragment. This single band actually represents 4 overlapping, yet discrete peptides: 2, approximately 25-kDa light chains as seen in the whole-antibody sample, as well as 2 partially digested heavy chains cleaved at the hinge region, also measuring approximately 25 kDa.

Whole-Antibody and F(ab′)2 Affinity

Independent dissociation constant (K_d) measurements were performed in triplicate using a ForteBio OctetRED96 (Pall Life Sciences). Results were internally consistent and demonstrated a K_d of approximately 30 pM for both the whole αGPC3 and the F(ab′)2 fragment.

Radiochemistry

Overall, 94.5% of the reaction activity (7.5 mL) was recovered from the reaction mixture and rinses applied to the purification PD-10 column. A heart-cut of fractions with maximal activity was pooled and sterilized by micron filtration (153 MBq; 39% radiochemical yield; 97.7% specifically bound activity by instant thin-layer chromatography). The specific activity of the labeled antibody was 75 MBq/mg, assuming 85% protein recovery from the column. The formulated dose was subsequently used for small-animal PET studies in tumor-bearing mice.

Tissue Biodistribution

In vivo tissue biodistribution was evaluated 4, 24, and 72 h after administration of ^{89}Zr-αGPC3-F(ab′)2 (Fig. 2). Whole-antibody biodistribution measurements noted below are historic values (*9*). Though significantly lower than ^{89}Zr-αGPC3 values observed in previous studies, tumor uptake of ^{89}Zr-αGPC3-F(ab′)2 was higher than any other tissue, peaking at 100 ± 21 percentage injected dose per gram (%ID/g) at 24 h. Tumor uptake ranged from 33- to 38-fold higher in HepG2 tumor–bearing animals relative to RH7777 controls. In contrast to ^{89}Zr-αGPC3, which demonstrated a blood-pool half-life of around 5 d, ^{89}Zr-αGPC3-F(ab′)2 was rapidly cleared from the blood, falling from 16 ± 6.7 %ID/g at 4 h to 3.5 ± 1.2 %ID/g at 24 h and ultimately 0.4 ± 0.1 %ID/g at 72 h, constituting a blood half-life of approximately 11 h The kidneys exhibited the highest nontumor organ uptake, peaking at 83 ± 12 %ID/g 24 h after injection, whereas peak liver activity (5.5 ± 1.1 %ID/g) was considerably lower than that observed with whole-antibody conjugate (21 ± 5.3 %ID/g). Tissue uptake in the bone, brain, cecum, heart, lungs, muscle, and spleen remained below 7 %ID/g throughout the duration of the study.

Small-Animal PET Imaging

Animals were selected for small-animal PET imaging on the basis of the presence of orthotopic xenografts as validated by IVIS imaging (Fig. 3A). The smallest HepG2 tumor measured 1.5 mm at necropsy and was clearly visible on PET at all 3 imaging times (4, 24, and 72 h) on both axial and coronal sections (Fig. 3B), with tumor uptake peaking at 24 h at 67 ± 13 %ID/g. This measurement from the PET images was not corrected for partial-volume effect, suggesting uptake by this small lesion was likely higher. The largest HepG2 tumor (7 mm) demonstrated peak uptake of 98 ± 19 %ID/g at 24 h by PET. All 3 HepG2 tumor–bearing animals cotreated with 1 mg of unlabeled αGPC3 possessed tumors similar in size to the large HepG2 animal, as validated by IVIS (Fig. 3) and necropsy. The tumor blocked with unlabeled αGPC3 was not evident on PET imaging at any time point; thus, uptake was assumed to be approximately equal to background liver signal (6.2 ± 1.4 %ID/g). Interestingly, large GPC3-negative RH7777 tumors were visible on PET as negative images (Fig. 3B), indicating that ^{89}Zr-αGPC3-F(ab′)2 uptake was lower than the surrounding liver tissue and thus minimizing concerns regarding nonspecific tumor binding due to the enhanced permeability retention effect.

^{89}Zr-αGPC3-F(ab′)2 demonstrated markedly different in vivo biodistribution and pharmacokinetics when compared with historic ^{89}Zr-αGPC3 controls (Fig. 4). Peak tumor uptake for the F(ab′)2

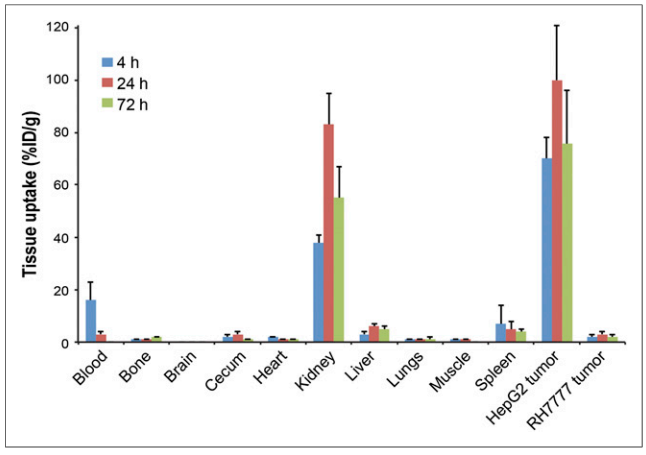

FIGURE 2. Tissue biodistribution of ^{89}Zr-αGPC3-F(ab′)2 measured by Cobra II γ counter in tumor-bearing mice (n = 5 each).

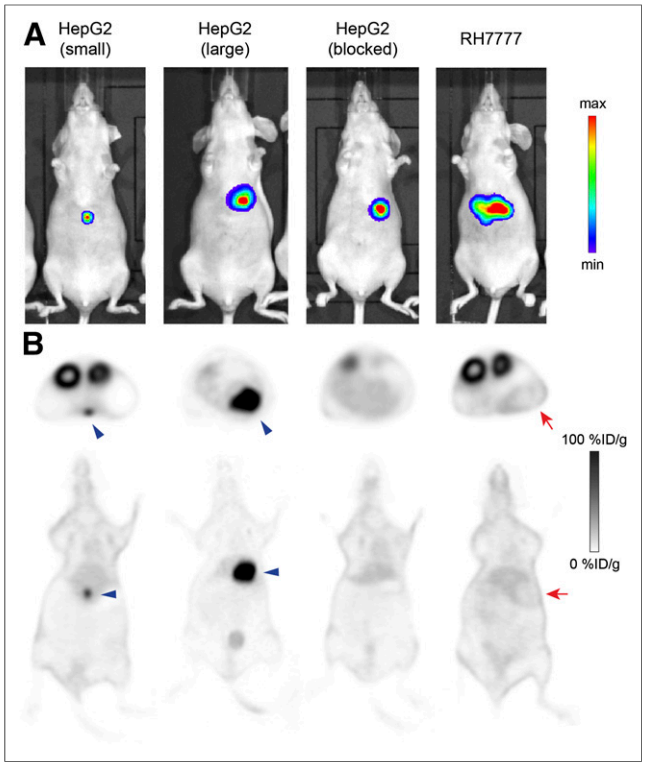

FIGURE 3. (A) IVIS luminescent images after intraperitoneal administration of luciferin (75 mg/kg) verifying presence of intrahepatic tumor before administration of ^{89}Zr-F(ab′)2. (B) Axial and coronal PET images of same animals (24 h) demonstrating tumor concordance in HepG2 animals and absence of PET signal in RH7777 tumors and blocked HepG2 controls. Blue arrowheads indicate HepG2 tumors; red arrows indicate RH7777 tumors. max = maximum; min = minimum.

conjugate was significantly lower than that for the whole-antibody conjugate (100 ± 21 %ID/g, compared with 837 ± 87 %ID/g). ^{89}Zr-αGPC3-F(ab′)2 exhibited relatively small changes in tumor uptake over the first 72 h, rising 30 %ID/g between the 4- and 24-h imaging times and then falling 24.3 %ID/g between the 24- and 72-h imaging sessions. Conversely, ^{89}Zr-αGPC3 tumor uptake continually rose over the first 72 h, increasing roughly 400 %ID/g between the first 3 imaging times. Background liver signal was significantly lower with ^{89}Zr-αGPC3-F(ab′)2, ranging from 3.2 ± 0.2 %ID/g at 4 h to 5.9 ± 0.4 %ID/g at 24 h, whereas historic ^{89}Zr-αGPC3 controls showed normal liver uptake in the 14–24 %ID/g range. This substantial decrease in background liver signal with ^{89}Zr-αGPC3-F(ab′)2 resulted in a superior tumor-to-liver contrast ratio (23.3) over that observed with ^{89}Zr-αGPC3 (1.2) at 4 h. The decrease in background liver signal led to clearly visible tumors on PET at 4 h, whereas animals treated with ^{89}Zr-αGPC3 exhibited no visible tumor at this time point (Fig. 4). Because of the remarkably high tumor uptake at 72 h, ^{89}Zr-αGPC3 ultimately achieved a superior tumor-to-liver ratio (30.5) at 72 h; however, even at this later time point the tumor-to-liver contrast ratio for ^{89}Zr-αGPC3-F(ab′)2 was 15.1.

DISCUSSION

Accurate diagnostic imaging is the foundation on which the diagnosis and therapeutic plan for HCC are built. As previously reported, ^{89}Zr-αGPC3 PET addresses many of the limitations encountered with the current standard multiphase CT and MR imaging in the radiographic diagnosis of HCC but is not without its shortcomings (*9*). In general, mAb-conjugated imaging probes have long blood half-lives, poorer tumor penetration, and relatively increased immunogenicity when compared with smaller targeting moieties. This proof-of-concept study demonstrates the feasibility of conjugating ^{89}Zr to F(ab′)2 fragments targeting the HCC-specific cell surface proteoglycan GPC3 in an attempt to address some of the limitations imposed by mAbs and demonstrate in vivo hepatic tumor localization.

The generation of Fab and F(ab′)2 fragments from the digestion of parent IgG_1 has been described using several enzymes including papain, pepsin, and ficin (*34*). Immobilized ficin was chosen for this work as previous studies have demonstrated the affinity of resultant fragments to be comparable to that of the parent antibody (*35*). The αGPC3 digestion product was subjected to HPLC instead of standard protein A purification to ensure purity and homogeneity of the F(ab′)2 used for radiolabeling. HPLC is unable to discriminate between noncovalently bonded Fab that mimics F(ab′)2 and true F(ab′)2; therefore, the isolated fractions were subjected to heat-denaturing without reduction and evaluated on SDS-PAGE (Fig. 1D) to verify the presence of a true F(ab′)2 fragment. There is evidence on the postradiolabeling HPLC tracing that a minority larger-molecular-weight population is created during the radiolabeling process, likely representing dimerization (Fig. 1C), a phenomenon observed after each of the radiolabeling trials. The relatively high absolute tumor uptake combined with the fact that the larger-molecular-weight species represented a small fraction of the total injected dose diminishes the likelihood that this population played a significant role in the radiotracer's in vivo performance.

One of the primary drivers of this work was to evaluate whether the creation of αGPC3-F(ab′)2 would indeed hasten in vivo clearance to enable imaging at earlier time points. Previous studies in the field demonstrated that blood clearance of mAb fragments was inversely related to their size (*36*), whereas Covell et al. reported murine IgG was retained 17 times longer than F(ab′)2 in vivo (*25*). ^{89}Zr-αGPC3-F(ab′)2 demonstrated a 10-fold reduction in blood half-life, compared with ^{89}Zr-αGPC3 (Table 1), retaining only 0.4 %ID/g activity in blood at 72 h, relative to 13 %ID/g in ^{89}Zr-αGPC3 historic controls (*9*). This was in conjunction with a reduction of background liver uptake in the ^{89}Zr-αGPC3-F(ab′)2–treated animals (5.5 vs. 21%IDg), further enabling hepatic tumor localization. This reduction in background liver signal was not solely due to decreased blood-pool activity, because liver activity was measured on ringers-perfused (nonbloody-containing) tissues.

We originally hypothesized that reduction in liver tumor binding would primarily result from decrease in F(ab′)2 affinity for GPC3. However, as evidenced by the ForteBio K_d results, αGPC3-F(ab′)2 retains excellent subnanomolar binding affinity equivalent to that of parent αGPC3. The marked reduction in peak absolute tumor uptake of F(ab′)2 is therefore not likely due to a reduction in the radioconjugate's tumor affinity but rather the significantly diminished blood circulation time, giving the radioconjugate less time to interact with tumor tissue as it rapidly clears from the body. Despite this lower absolute tumor uptake, ^{89}Zr-αGPC3-F(ab′)2 was still able to achieve a high tumor-to-liver ratio (23.3) at 4 h because of low background blood and liver activity. This tumor-to-background ratio is still superior to most whole-antibody–targeted PET probes, with peak signal-to-background ratios in the 1.5–4 range (*37*). It was also a prestudy consideration that the smaller size of ^{89}Zr-αGPC3-F(ab′)2 would lead to increased susceptibility to the effects of enhanced permeability retention in tumors and therefore increased nonspecific binding.

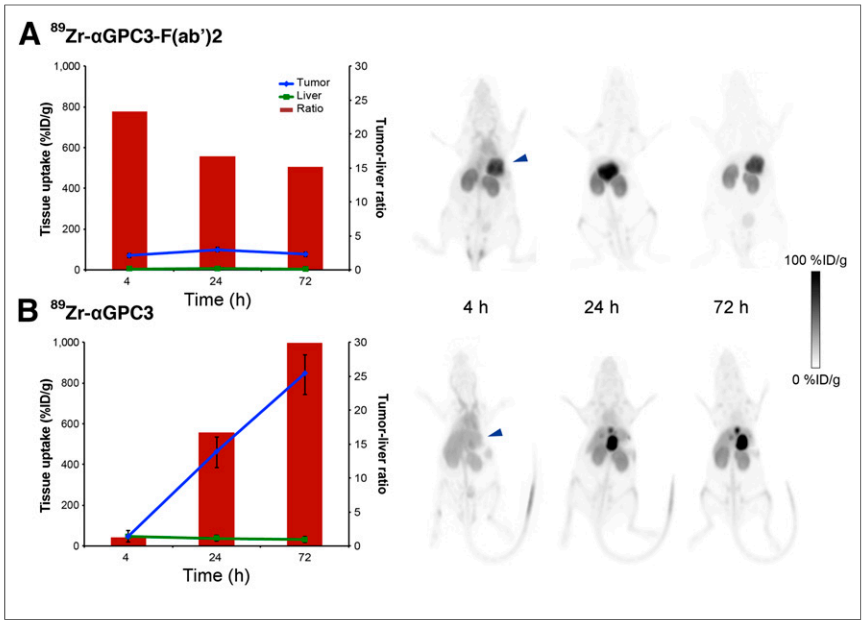

FIGURE 4. Tumor-to-liver tissue uptake (line graphs), tumor-to-liver contrast ratios (bar graphs), and representative PET images in HepG2-bearing mice injected with ^{89}Zr-αGPC3-F(ab′)2 (A) and ^{89}Zr-αGPC3 (B). Signal saturation was allowed in ^{89}Zr-αGPC3 animal images to allow comparison with ^{89}Zr-αGPC3-F(ab′)2. (Data from B has been reprinted with permission of (*9*).)

The absence of uptake in large non–antigen-expressing RH7777 tumors diminishes this concern, because PET images of these tumors actually show signal lower than background liver tissue (Fig. 3B).

Because the use of F(ab′)2 significantly reduces blood circulation time, the choice of ^{89}Zr for use in the PET probe must be carefully considered. Indeed, ^{89}Zr was originally selected as a viable immuno-PET radionuclide because of its relatively long half-life (78.4 h) and ability to outlast whole-antibody clearance in vivo for use in PET imaging (*38*). However, other shorter-half-life radionuclides such as ^{18}F and ^{68}Ga could be used in an attempt to reduce patient radiation exposure. ^{18}F has a range uncertainty similar to ^{89}Zr (maximum, ~2.4 mm; average, ~0.8 mm), maintaining theoretic spatial resolution; however, conjugation with targeting peptides has proven more complex (*39*).

The risk of using a long-half-life radioisotope with αGPC3-F(ab′)2 fragments is compounded by the concentration of the fragments (and subsequent radioisotopes should they be conjugated) in the kidneys, elevating the potential risk of organ dysfunction in the clinical setting. Elevated renal uptake does not, however, preclude peptide-targeted radionuclides from clinical use. ^{111}In-octreotide scintigraphy is widely used clinically despite demonstrating high renal uptake (*40*). In the case of ^{89}Zr-αGPC3-F(ab′)2, clinical utility would likely be maintained because HCC rarely metastasizes to the kidneys (*41*). Gelatin-based plasma expanders have been used in conjunction with ^{111}In-octreotide to reduce kidney retention and renal irradiation (*42*), thus demonstrating the feasibility of renal-protective adjuncts when administering peptide-targeted tracers. A similar approach could be used to reduce renal uptake of αGPC3-F(ab′)2 while taking advantage of its favorable early tumor-to-liver contrast.

As a proof-of-concept study for the use of F(ab′)2 for immuno-PET in an immunocompromised nude mouse model of HCC, the murine immune response to αGPC3 or αGPC3-F(ab′)2 could not be evaluated. Although αGPC3-F(ab′)2 is likely less immunogenic than whole αGPC3 because of the absence of the Fc region, further evaluation of its immune reactivity would be needed before clinical implementation. Although the results of this preclinical study are encouraging, further clinical translation would require use of a humanized form of αGPC3, which could be achieved through de novo development of humanized αGPC3 or use of one of several existing humanized GPC3-targeting mAbs (*43*).

Ultimately, ^{89}Zr-αGPC3-F(ab′)2 addresses several of the limitations imposed by whole-antibody–based ^{89}Zr-αGPC3. Its faster blood clearance and lower background liver uptake allow for early imaging of GPC3-expressing liver tumors despite significantly lower absolute tumor uptake. However, kidney uptake is significant, potentially limiting repeated clinical doses. Additionally, ^{89}Zr-αGPC3 has considerably higher absolute tumor uptake and ultimately achieves higher tumor-to-liver ratios at later time points. These differences are important to consider during radioconjugate development, though their clinical significance is yet unknown. One potential approach would be taking advantage of αGPC3-F(ab′)2's faster clearance for use in diagnostic imaging, followed by whole αGPC3's high absolute tumor uptake for therapeutic radioisotope (e.g., ^{90}Y, ^{211}At, ^{177}Lu) delivery as an adjuvant treatment modality. As new mAb therapies are developed, either agent may enable noninvasive evaluation of tumor GPC3 expression status or response to treatment.

CONCLUSION

In this follow-up preclinical study, ^{89}Zr-αGPC3-F(ab′)2 was able to clearly identify orthotopic GPC3–expressing HCC tumors with high signal-to-noise ratio. The use of F(ab′)2 for tumor targeting is feasible, resulted in faster blood clearance, and enabled earlier imaging when compared with whole-antibody conjugates; however,

TABLE 1
Pertinent Characteristics of ^{89}Zr-αGPC3 and ^{89}Zr-αGPC3-F(ab′)2

Probe	Molecular weight* (kDa)	K_d* (nM)	Blood half-life (h)	Tumor-to-liver ratio at 4 h	Tumor-to-liver ratio at 72 h
^{89}Zr-αGPC3	~155	0.03	115	1.2	30.5
^{89}Zr-αGPC3-F(ab′)2	~110	0.03	11	23.2	15.1

*Measurements were performed on whole mAb and F(ab′)2 prior to conjugation with isothiocyanotobenzyldesferrioxamine.

absolute tumor uptake was lower. ^{89}Zr-αGPC3-F(ab′)2 addresses some of the shortcomings of whole-antibody immuno-PET probes, however, further studies are needed to fully characterize the benefits of each to determine the optimal targeting agent for both diagnostic and therapeutic isotope delivery in HCC.

DISCLOSURE

The costs of publication of this article were defrayed in part by payment of page charges. Therefore, and solely to indicate this fact, this article is hereby marked "advertisement" in accordance with 18 USC section 1734. Financial support for this study was received from NCI grant T32CA138312, the University of Washington Department of Surgery reinvestment grant, and the American Brain Tumor Association Basic Research Fellowship in Honor of Susan Kramer. The content is solely the responsibility of the authors and does not necessarily represent the official views of the NCI or NIH. No other potential conflicts of interest relevant to this article are reported.

ACKNOWLEDGMENTS

We thank Gregory Garwin and Barbara Lewellen for technical assistance with the small-animal PET studies.

REFERENCES

1. Ferenci P, Fried M, Labrecque D, et al. Hepatocellular carcinoma (HCC) a global perspective. *J Clin Gastroenterol.* 2010;44:239–245.
2. International Agency for Research on Cancer. GLOBOCAN 2012: Estimated Cancer Incidence, Mortality and Prevalence Worldwide in 2012. International Agency for Research on Cancer website. http://globocan.iarc.fr/Pages/fact_sheets_population.aspx. Accessed October 1, 2014.
3. National Comprehensive Cancer Network. Hepatobiliary Cancers Version 2.2014. National Comprehensive Cancer Network website. http://www.nccn.org/professionals/physician_gls/pdf/hepatobiliary.pdf. Accessed October 1, 2014.
4. ACR. LI-RADS v2013.1. ACR website. http://www.acr.org/~/media/ACR/Documents/PDF/QualitySafety/Resources/LIRADS/lirads v20131.pdf. Accessed September 22, 2014.
5. Ayyappan AP, Jhaveri KS. CT and MRI of hepatocellular carcinoma: an update. *Expert Rev Anticancer Ther.* 2010;10:507–519.
6. Sangiovanni A, Manini MA, Iavarone M, et al. The diagnostic and economic impact of contrast imaging techniques in the diagnosis of small hepatocellular carcinoma in cirrhosis. *Gut.* 2010;59:638–644.
7. Colli A, Fraquelli M, Casazza G, et al. Accuracy of ultrasonography, spiral CT, magnetic resonance, and alpha-fetoprotein in diagnosing hepatocellular carcinoma: a systematic review. *Am J Gastroenterol.* 2006;101:513–523.
8. Golfieri R, Marini E, Bazzocchi A, et al. Small (<or=3 cm) hepatocellular carcinoma in cirrhosis: the role of double contrast agents in MR imaging vs. multidetector-row CT. *Radiol Med (Torino).* 2009;114:1239–1266.
9. Sham JG, Kievit FM, Grierson JR, et al. Glypican-3-targeted ^{89}Zr PET imaging of hepatocellular carcinoma. *J Nucl Med.* 2014;55:799–804.
10. Primus FJ, Bennett SJ, Kim EE, DeLand FH, Zahn MC, Goldenberg DM. Circulating immune complexes in cancer patients receiving goat radiolocalizing antibodies to carcinoembryonic antigen. *Cancer Res.* 1980;40:497–501.
11. Milenic DE, Detrick B, Reynolds JC, Colcher D. Characterization of primate antibody responses to administered murine monoclonal immunoglobulin. *Int J Biol Markers.* 1990;5:177–187.
12. Jain RK. Transport of molecules in the tumor interstitium: a review. *Cancer Res.* 1987;47:3039–3051.
13. Goel A, Baranowska-Kortylewicz J, Hinrichs SH, et al. ^{99m}Tc-labeled divalent and tetravalent CC49 single-chain Fv's: novel imaging agents for rapid in vivo localization of human colon carcinoma. *J Nucl Med.* 2001;42:1519–1527.
14. Britton KE. The development of new radiopharmaceuticals. *Eur J Nucl Med.* 1990;16:373–385.
15. Wong KJ, Baidoo KE, Nayak TK, Garmestani K, Brechbiel MW, Milenic DE. In vitro and in vivo pre-clinical analysis of a F(ab′)(2) fragment of panitumumab for molecular imaging and therapy of HER1 positive cancers. *EJNMMI Res.* 2011;1.
16. Stafford JH, Hao G, Best AM, Sun X, Thorpe PE. Highly specific PET imaging of prostate tumors in mice with an iodine-124-labeled antibody fragment that targets phosphatidylserine. *PLoS ONE.* 2013;8:e84864.
17. Oude Munnink TH, de Vries EG, Vedelaar SR, et al. Lapatinib and 17AAG reduce ^{89}Zr-trastuzumab-F(ab′)2 uptake in SKBR3 tumor xenografts. *Mol Pharm.* 2012;9:2995–3002.
18. Ma T, Sun X, Cui L, et al. Molecular imaging reveals trastuzumab-induced epidermal growth factor receptor downregulation in vivo. *J Nucl Med.* 2014;55:1002–1007.
19. Hoeben BA, Kaanders JH, Franssen GM, et al. PET of hypoxia with ^{89}Zr-labeled cG250-F(ab′)2 in head and neck tumors. *J Nucl Med.* 2010;51:1076–1083.
20. Beylergil V, Morris PG, Smith-Jones PM, et al. Pilot study of ^{68}Ga-DOTA-F(ab′)2-trastuzumab in patients with breast cancer. *Nucl Med Commun.* 2013;34:1157–1165.
21. Milenic DE, Esteban JM, Colcher D. Comparison of methods for the generation of immunoreactive fragments of a monoclonal antibody (B72.3) reactive with human carcinomas. *J Immunol Methods.* 1989;120:71–83.
22. Yokota T, Milenic DE, Whitlow M, Schlom J. Rapid tumor penetration of a single-chain Fv and comparison with other immunoglobulin forms. *Cancer Res.* 1992;52:3402–3408.
23. Wu AM. Antibodies and antimatter: the resurgence of immuno-PET. *J Nucl Med.* 2009;50:2–5.
24. Wahl RL, Parker CW, Philpott GW. Improved radioimaging and tumor localization with monoclonal F(ab')2. *J Nucl Med.* 1983;24:316–325.
25. Covell DG, Barbet J, Holton OD, Black CD, Parker RJ, Weinstein JN. Pharmacokinetics of monoclonal immunoglobulin G1, F(ab′)2, and Fab′ in mice. *Cancer Res.* 1986;46:3969–3978.
26. Dijkers EC, Oude Munnink TH, Kosterink JG, et al. Biodistribution of ^{89}Zr-trastuzumab and PET imaging of HER2-positive lesions in patients with metastatic breast cancer. *Clin Pharmacol Ther.* 2010;87:586–592.
27. Dijkers EC, Kosterink JG, Rademaker AP, et al. Development and characterization of clinical-grade ^{89}Zr-trastuzumab for HER2/neu immunoPET imaging. *J Nucl Med.* 2009;50:974–981.
28. Nayak TK, Garmestani K, Milenic DE, Brechbiel MW. PET and MRI of metastatic peritoneal and pulmonary colorectal cancer in mice with human epidermal growth factor receptor 1-targeted ^{89}Zr-labeled panitumumab. *J Nucl Med.* 2012;53:113–120.
29. Chames P, Van Regenmortel M, Weiss E, Baty D. Therapeutic antibodies: successes, limitations and hopes for the future. *Br J Pharmacol.* 2009;157:220–233.
30. Elgqvist J, Andersson H, Jensen H, et al. Repeated Intraperitoneal alpha-Radioimmunotherapy of Ovarian Cancer in Mice. *J Oncol.* 2010;2010:394913.
31. Wayner EA, Hoffstrom BG. Development of monoclonal antibodies to integrin receptors. *Methods Enzymol.* 2007;426:117–153.
32. Vosjan MJ, Perk LR, Visser GW, et al. Conjugation and radiolabeling of monoclonal antibodies with zirconium-89 for PET imaging using the bifunctional chelate p-isothiocyanatobenzyl-desferrioxamine. *Nat Protoc.* 2010;5:739–743.
33. Gage GJ, Kipke DR, Shain W. Whole animal perfusion fixation for rodents. *J Vis Exp.* 2012;65:e3564.
34. Rousseaux J, Rousseaux-Prevost R, Bazin H. Optimal conditions for the preparation of Fab and F(ab')2 fragments from monoclonal IgG of different rat IgG subclasses. *J Immunol Methods.* 1983;64:141–146.
35. Mariani M, Camagna M, Tarditi L, Seccamani E. A new enzymatic method to obtain high-yield F(ab)2 suitable for clinical use from mouse IgGl. *Mol Immunol.* 1991;28:69–77.
36. Milenic DE, Yokota T, Filpula DR, et al. Construction, binding properties, metabolism, and tumor targeting of a single-chain Fv derived from the pancarcinoma monoclonal antibody CC49. *Cancer Res.* 1991;51:6363–6371.
37. Marquez BV, Zheleznyak A, Lapi SE. Glypican-3-targeted ^{89}Zr PET imaging of hepatocellular carcinoma: where antibody imaging dares to tread. *J Nucl Med.* 2014;55:708–709.
38. Zhang Y, Hong H, Cai W. PET tracers based on zirconium-89. *Curr Radiopharm.* 2011;4:131–139.
39. Liu K, Lepin EJ, Wang MW, et al. Microfluidic-based ^{18}F-labeling of biomolecules for immuno-positron emission tomography. *Mol Imaging.* 2011;10:168–176.
40. Rolleman EJ, Kooij PP, de Herder WW, Valkema R, Krenning EP, de Jong M. Somatostatin receptor subtype 2-mediated uptake of radiolabelled somatostatin analogues in the human kidney. *Eur J Nucl Med Mol Imaging.* 2007;34:1854–1860.
41. D'Antonio A, Caleo A, Caleo O, Addesso M, Boscaino A. Hepatocellular carcinoma metastatic to the kidney mimicking renal oncocytoma. *Hepatobiliary Pancreat Dis Int.* 2010;9:550–552.
42. Vegt E, Wetzels JF, Russel FG, et al. Renal uptake of radiolabeled octreotide in human subjects is efficiently inhibited by succinylated gelatin. *J Nucl Med.* 2006;47:432–436.
43. Zhu AX, Gold PJ, El-Khoueiry AB, et al. First-in-man phase I study of GC33, a novel recombinant humanized antibody against glypican-3, in patients with advanced hepatocellular carcinoma. *Clin Cancer Res.* 2013;19:920–928.